Available online at www.sciencedirect.com
ScienceDirect
Journal of Hazardous Materials 140 (2007) 504–517
Journal of Hazardous Materials
www.elsevier.com/locate/jhazmat

On the application of computational fluid dynamics codes for liquefied natural gas dispersion

Anay Luketa-Hanlin [a,*], Ronald P. Koopman [b,1,2], Donald L. Ermak [c,2]

[a] *Sandia National Laboratories, Fire Science and Technology Department, P.O. Box 5800, MS-1135, Albuquerque, NM 87185, United States*
[b] *Hazard Analysis Consulting, 4673 Almond Circle Livermore, CA 94550, United States*
[c] *Lawrence Livermore National Laboratory, United States*

Available online 13 October 2006

Abstract

Computational fluid dynamics (CFD) codes are increasingly being used in the liquefied natural gas (LNG) industry to predict natural gas dispersion distances. This paper addresses several issues regarding the use of CFD for LNG dispersion such as specification of the domain, grid, boundary and initial conditions. A description of the k–ε model is presented, along with modifications required for atmospheric flows. Validation issues pertaining to the experimental data from the Burro, Coyote, and Falcon series of LNG dispersion experiments are also discussed. A description of the atmosphere is provided as well as discussion on the inclusion of the Coriolis force to model very large LNG spills.

Keywords: Liquefied natural gas; CFD; Dispersion; k–ε model; Validation

1. Introduction

When liquefied natural gas (LNG) is spilled onto land or water, it rapidly vaporizes to form a natural gas cloud. One of the requirements in performing a hazard analysis related to a LNG spill is to determine the maximum extent from the spill at which the lower flammability limit (LFL) is reached within the natural gas cloud. One tool that is being increasingly used in industry for LNG dispersion modeling is computational fluid dynamics (CFD) codes. This paper addresses boundary and initial condition treatment when using CFD codes for this application, as well as validation issues and requirements.

The main purpose of this paper is to provide a useful assembly of available information so that the sectors of industry using CFD for this application will have a convenient reference for guidance. The focus will be on the k–ε model for turbulent transport since this model is the one most commonly available in commercial codes. Relative to other models, such as large eddy simulation (LES) or algebraic stress models, it has a low computational cell requirement and has fast computational run times. Hence, codes using this model can be run on single processors in a reasonable length of run time.

It is instructive to describe the nature of a natural gas cloud to give an understanding of what features are required in a model. Since LNG is a cryogen at a temperature of 111 K (−260 °F), it rapidly vaporizes when it is spilled onto land or water at a much higher temperature. The natural gas cloud is usually visible due to entrainment and consequent condensation of water vapor in the atmosphere. The evolving vapor propagates downwind at roughly the wind speed or less, depending on cloud size and atmospheric stability and has a very low height to lateral dimension ratio due to the vapor density which is initially 1.5 times that of air. The density decreases as air is mixed in and cooled, principally at the peripheral regions of the cloud so that the cloud's core will be at the lowest temperature and hence the highest density. As the cloud moves downwind, air mixes with the cold LNG vapor, which cools the air, keeping the mixture denser than the ambient air even though the LNG vapor itself may be slightly less dense than the ambient air. Eventually the LNG vapor cloud will be completely mixed with air and will dilute. The only mechanism for the cloud to become buoyant under extremely low wind speeds and very stable conditions will be by contact with the ground or water surface allowing for the cloud to lift off the surface from the heat transfer. Natural gas vapors must be at 166 K (−160 °F) to be neutrally buoyant in air at 289 K (60 °F).

* Corresponding author. Tel.: +1 505 284 8280; fax: +1 505 845 3151.
E-mail addresses: aluketa@sandia.gov (A. Luketa-Hanlin), rpkoopman@comcast.net (R.P. Koopman).
[1] Tel.: +1 925 443 5324.
[2] Retired from Lawrence Livermore National Laboratory.

0304-3894/$ – see front matter © 2006 Elsevier B.V. All rights reserved.
doi:10.1016/j.jhazmat.2006.10.023

Nomenclature

c_p	Specific heat at constant pressure (J/(kg K))
CFD	computational fluid dynamics
d	displacement length (m)
DNS	direct numerical simulation
E	mass flux of water vapor (kg/(m^2 s))
f	Coriolis parameter (s^{-1})
h	planetary boundary layer height (m)
H	sensible heat flux (W/m^2)
k	turbulent kinetic energy (m^2/s^2)
K_h	eddy diffusivity of heat (m^2/s)
K_m	eddy viscosity (m^2/s)
L	Obuhkov length (m)
LES	large eddy simulation
LFL	lower flammability limit
LNG	liquefied natural gas
p	exponent of power law function
P	pressure (Pa)
P_0	reference pressure (Pa)
PBL	planetary boundary layer
q_*	specific humidity scale (kg water vapor/kg air)
Q	specific humidity (kg water vapor/kg air)
Q_o	specific humidity at z_o (kg water vapor/kg air)
RANS	Reynolds Averaged Navier–Stokes
Ri	Richardson number
Ro	Rossby number
RPT	rapid phase transition
R_s	Reynolds-stress tensor
T	temperature (K)
T_*	temperature scale (K)
u_*	friction velocity (m/s)
U	x-component velocity (m/s)
U_g	geostrophic x-component velocity (m/s)
U_r	reference velocity (m/s)
v_g	gas phase velocity at LNG pool surface (m/s)
V	y-component velocity (m/s)
V_g	geostrophic y-component velocity (m/s)
W	z-component velocity (m/s)
z	vertical coordinate
z_o	surface roughness length (m)
z_r	reference height (m)

Greek letters

ε	turbulence dissipation rate (m^2/s^3)
Γ	adiabatic lapse rate (K/m)
φ	latitude (°)
κ	von Karman constant (∼0.4)
θ	potential temperature (K)
θ_o	potential temperature at z_o (K)
ρ	density (kg/m^3)
ρ_g	gas phase density at LNG pool surface (kg/m^3)
Ω	rotational speed of the Earth (s^{-1})

Since LNG is comprised primarily of methane (85–95 vol%) the lower flammability limit of interest is that of methane whose LFL is 5% concentration by volume, or alternatively 2.76% by mass in air. The conversion factor between the two is the ratio of molecular weights of methane to air. The distinction of whether the concentration is by volume or mass is very important since codes can have default units with can be either one of these.

The maximum distance to the LFL is mainly a function of spill rate, atmospheric conditions, and the presence of obstacles or terrain features. The maximum distance to LFL will increase for increasing spill rate. At a particular spill rate, initially the cloud will propagate downwind and the LFL distance will increase until a steady state is reached where the evaporation rate matches the spill rate. At this point the maximum distance to LFL is affected only by fluctuations in atmospheric conditions or obstacles. At a given spill rate, atmospheric conditions significantly affect dispersion distances. Typically, the classification of 'stable' and low wind speeds will result in the furthest distance to the LFL. Classifications, which characterize atmospheric conditions, will be described in a later section. When obstacles or terrain features are present they can either result in flow patterns which enhance gravity flow, increasing LFL distance, or increase mixing or provide containment which will reduce the distance to LFL.

Hence, from the above description it is evident that turbulent mixing of the cloud with the atmosphere, either through buoyancy, shear or other mechanical driven mechanisms, is a feature that must be adequately modeled in a CFD code, as well as the heat transfer that occurs between the much lower temperature cloud, the atmosphere, and the surface. The following section describes characteristics and classifications of the atmosphere and the effect on maximum distance to LFL. Then a description of the standard k–ε turbulence model and required modifications for atmospheric flows is provided, followed by a discussion on computational specifications such as boundary and initial conditions. Finally, validation using experimental data obtained from the Burro, Coyote, and Falcon test series are discussed.

2. Description of the atmosphere

There are several sources providing discussion and review of the characteristics of the atmosphere [1–6]. A brief description is given here to aid in the discussion to follow on the application of boundary and initial conditions. The atmospheric or planetary boundary layer (PBL) is defined as the layer in which Earth's surface affects the atmosphere through momentum, heat, and moisture exchange occurring over time scales of a few hours to less than a day [1]. The PBL is the region of interest for LNG dispersion in light of the typical volumes (∼200,000–300,000 m^3) of LNG contained in facilities currently being considered and the possible cloud heights and dispersion time scales from such spills. The height of the PBL varies, depending on several factors such as heat exchange between the Earth's surface and the atmosphere, wind speed, surface roughness, and topographical characteristics. The height can vary between tens of meters to several kilometers and will typically be between roughly 250 m

in the morning and 0.2 and 5 km during the late afternoon [1]. The top of the PBL is usually defined as the height at which turbulent motion is not significant. The lowest part of the PBL, roughly 10%, is called the surface layer in which momentum, heat, and moisture vertical fluxes do not vary by more than 10% [5]. Due to the small flux variations the surface layer has been amenable to similarity theories such as the Monin–Obukhov scaling theory, applicable only to the surface layer.

The condition of the PBL is classified as either unstable, neutral, or stable. When turbulence generation dominates, produced either through unstable stratification or mechanical effects, the PBL is in an unstable condition. In neutral conditions, buoyancy influences are not significant, and the temperature profile decreases upwards at the adiabatic lapse rate defined as a vertical temperature distribution in which an upward moving fluid particle will always be at the local temperature. For thermal instability to occur, the temperature profile must decrease at a rate greater than the adiabatic lapse rate [7]. Stable conditions correspond to the damping of turbulent motion, which can occur through stable temperature or density gradients. Stable conditions usually occur in conjunction with low speeds (~2–4 m/s) and typically during the night or early morning, while unstable conditions usually occur during the day.

These conditions have been characterized by several methods. The most popular is the Pasquill–Gifford stability classes (A–F) [8], with 'A' corresponding to extremely unstable and 'F' to moderately stable conditions. The stability condition of the atmosphere significantly affects the dispersion of the natural gas (NG) cloud. It has been found from experiment [9] that stable atmospheric conditions (E, F) with low speeds results in the greatest LFL distances. This is due to the suppression of turbulence from stable stratification, hence mixing is suppressed and the cloud propagates further downwind before diluting.

Of prime importance when performing a CFD simulation is using appropriate boundary and initial conditions. For LNG dispersion, this involves obtaining representative profiles of velocity, temperature, and humidity of the atmosphere. As previously mentioned the Monin–Obukhov theory has provided a reasonable representation of the surface layer for all but 'very stable' conditions where turbulence becomes highly non-uniform and intermittent. The theory is based on the assumptions that the shear stress is constant in this layer, that mean variables are a function of height only, and is applicable to a horizontally homogeneous and stationary flow field. The surface layer extends to approximately 10% of the height, h, of the PBL which can be approximated by

$$h = 0.4\left(\frac{u_* L}{f}\right)^{1/2} \tag{1}$$

where u_* and L, to be defined shortly, are the friction velocity and Obuhkov length. The Coriolis parameter, f, is related to the rotational speed of the Earth, Ω ($\approx 7.292 \times 10^{-5}\ \mathrm{s}^{-1}$), and latitude, φ (°), as $f = 2\Omega \sin\varphi$.

The height is also sometimes defined as where the turbulent kinetic energy is 5% of its surface value [10]. The flux relations for velocity, potential temperature, and specific humidity, U, θ, and Q, respectively, in the surface layer can be represented by [1,6]:

$$\frac{\partial U}{\partial z} = \frac{u_*}{\kappa z}\phi_\mathrm{m}\left(\frac{z}{L}\right) \tag{2}$$

$$\frac{\partial \theta}{\partial z} = \frac{T_*}{\kappa z}\phi_\mathrm{h}\left(\frac{z}{L}\right) \tag{3}$$

$$\frac{\partial Q}{\partial z} = \frac{q_*}{\kappa z}\phi_\mathrm{w}\left(\frac{z}{L}\right) \tag{4}$$

where

$$u_* = \left(\frac{\tau}{\rho}\right)^{1/2}, \quad T_* = -\frac{H}{\rho c_p u_*}, \quad q_* = -\frac{E}{\rho u_*} \tag{5}$$

$$L = -\frac{u_*^3 \rho c_p T}{\kappa g H} \tag{6}$$

and τ, H, T, and E are the surface values of shear stress, sensible heat flux, temperature, and mass flux of water vapor, respectively. When significant evaporation occurs such as in ocean environments it is important to take into account the transfer of water vapor. Land environments with low evaporation, such as deserts with little vegetation, will not require Eq. (4). The scaling parameters u_*, T_*, and q_* are the velocity, temperature, and specific humidity scales. The von Karman constant, κ, has a value of around 0.4. The Obukhov length, L, has units of length and represents the height at which buoyant destruction and shear production of turbulence is on the same order. The specific heat at constant pressure, c_p, and the density, ρ, are evaluated near the surface. The potential temperature, θ, is related to temperature by:

$$\theta = T\left(\frac{P_0}{P}\right)^n \tag{7}$$

$$\frac{\partial \theta}{\partial z} = \frac{\theta}{T}\left(\frac{\partial T}{\partial z} + \Gamma\right) \cong \frac{\partial T}{\partial z} + \Gamma \tag{8}$$

where $n = 0.286$, P_0 a reference pressure, and Γ, the adiabatic lapse rate, equal to approximately 0.01 K/m for an unsaturated atmosphere.

The functions ϕ_m, ϕ_h, and ϕ_w in Eqs. (2)–(4) must be evaluated empirically. All of the ϕ relations are a function of the parameter, z/L, which represents the ratio of turbulence production of that due to shear versus buoyancy. Negative values of z/L indicate an unstable condition, while positive values indicate stable. It should be pointed out that the functional form of the ϕ equations has been well established, however, there is variation on what the constants are for these equations due to measurement errors and the ideal condition assumptions of the similarity theory. Thus, the following equations for ϕ_m, ϕ_h, ϕ_w, k, and ε should be interpreted as providing trends and order of magnitude estimates. For practical applications the following empirical relations can be used [6]:

$$\phi_\mathrm{m}^2 = \phi_\mathrm{h} = \phi_\mathrm{w} = \left(1 - 15\frac{z}{L}\right)^{-1/2}, \quad \text{for } \frac{z}{L} < 0 \tag{9}$$

$$\phi_\mathrm{m} = \phi_\mathrm{h} = \phi_\mathrm{w} = 1 + 5\frac{z}{L}, \quad \text{for } \frac{z}{L} \geq 0 \tag{10}$$

Once u_*, T_*, and q^* are evaluated, and Eqs. (9) and (10) substituted into Eqs. (2)–(4) and integrated, the velocity, temperature, and specific humidity profiles can be determined. These profiles can then be utilized as boundary and initial conditions for a CFD simulation. After the aforementioned substitutions and integration the following relations result:

$$\ln z - \psi_m = \frac{\kappa}{u_*} U + \ln z_o \tag{11}$$

$$\ln z - \psi_h = \frac{\kappa}{T_*}\theta - \frac{\kappa}{T_*}\theta_o + \ln z_o \tag{12}$$

$$\ln z - \psi_h = \frac{\kappa}{q_*} Q - \frac{\kappa}{q_*} Q_o + \ln z_o \tag{13}$$

where ψ_m and ψ_h are:

$$\psi_m = \int_{z_o}^{z} \left(\frac{1}{z} + \frac{\phi_m}{z}\right) dz \tag{14}$$

$$\psi_h = \int_{z_o}^{z} \left(\frac{1}{z} + \frac{\phi_h}{z}\right) dz \tag{15}$$

The limits of integration are from z_o to z, where z_o is the surface roughness length. The roughness length can vary between 10^{-4} m for calm open oceans to up to around 3 m for cities with tall buildings, and is usually determined from wind profile measurements. When there are tall obstacles, such as trees and buildings, a zero-plane displacement length, d, is introduced into the flux equations by replacing z with z–d. The displacement length provides a new reference level above the obstacles in which a logarithmic profile can be applied with $u = 0$ at $z = z_o + d$. Typically, d is roughly 70–80% of the obstacle height.

In practice u_*, T_*, and q_* are estimated from measurements of mean velocity, temperature, and humidity at two or more heights within the surface layer, which are significantly above roughness elements. There are several methods to calculate these scaling parameters [5,6]. One commonly used technique is the profile method, which involves measurements at more than two heights. First the Richardson number, Ri, as a function of z_m, defined as $z_m = \sqrt{z_1 z_2}$, is plotted from consecutive pairs of these measurements. The following expression for Ri can be used:

$$Ri = \frac{g}{T_0} z_m \frac{\partial\theta_v/\partial z}{(\partial u/\partial z)^2} \ln\left(\frac{z_2}{z_1}\right) \tag{16}$$

The virtual potential temperature, θ_v, in Eq. (16) takes into account the presence of water vapor in the air. It is defined as

$$\frac{\partial\theta_v}{\partial z} \cong \frac{\partial T_v}{\partial z} + \Gamma \tag{17}$$

where $T_v = T(1 + 0.61Q)$.

The gradients in Eq. (16) can be represented well with a logarithmic approximation for unstable conditions.

$$\frac{\partial\xi}{\partial z} \cong \frac{\Delta\xi}{z_m \ln(z_2/z_1)} \tag{18}$$

A linear approximation has been found to be more representative for stable conditions.

$$\frac{\partial\xi}{\partial z} \cong \frac{\xi_2 - \xi_1}{z_2 - z_1} \tag{19}$$

The Richardson number is related to z_m/L by

$$\frac{z_m}{L} = Ri, \quad Ri < 0 \text{ unstable} \tag{20}$$

$$\frac{z_m}{L} = \frac{Ri}{1 - 5Ri}, \quad 0 \le Ri < 0.2 \text{ stable} \tag{21}$$

Given a plot of Ri versus z_m for unstable conditions, or $Ri/(1-5Ri)$ versus z_m for stable conditions, Eqs. (20) and (21) can be used to determine the slope L.

The next step is to plot best-fitted lines of U versus $\ln z - \psi_m$, θ versus $\ln z - \psi_h$, Q versus $\ln z - \psi_h$ from which the slopes of Eqs. (11)–(13) can be found (i.e. κ/u_*, κ/T_*, and κ/q_*). This then allows for the determination of u_*, T_*, and q_*, and hence the surface fluxes from Eq. (5). The intercepts of Eqs. (11)–(13) can also be found in order to determine z_o, Q_o, and θ_o, the specific humidity and potential temperature at $z = z_o$, respectively.

The region above the surface layer (≈0.1 h) is termed the mixed layer where velocity, potential temperature, and specific humidity are essentially uniform in unstable conditions due to mechanical and buoyant mixing. Above this region for unstable conditions, the temperature gradient is positive which provides an elevated inversion layer. Mixing is suppressed in this layer and hence, it can be expected that this would be the limiting height of a dispersing medium such as a pollutant or NG cloud. Outside the PBL, velocities are governed by a geostrophic balance, that is, a balance between pressure gradients and the Coriolis force. Above the surface layer under stable conditions, the velocity field will be closer to that of a geostrophic balance since buoyant mixing is not as strong. The geostrophic velocities, U_g and V_g, horizontal x- and y-components, respectively, can be determined from pressure and temperature measurements by using the following relations:

$$U_g = -\frac{1}{\rho f}\frac{\partial P}{\partial y}, \qquad V_g = \frac{1}{\rho f}\frac{\partial P}{\partial x} \tag{22}$$

To take into account the baroclinic effect of horizontal temperature gradients, the following approximation is typically used to determine velocities as a function of height.

$$\frac{\partial U_g}{\partial z} = -\frac{g}{fT}\frac{\partial T}{\partial y} + \frac{U_g}{T}\frac{\partial T}{\partial z} \cong -\frac{g}{fT}\frac{\partial T}{\partial y} \tag{23}$$

$$\frac{\partial V_g}{\partial z} = \frac{g}{fT}\frac{\partial T}{\partial x} + \frac{V_g}{T}\frac{\partial T}{\partial z} \cong \frac{g}{fT}\frac{\partial T}{\partial x} \tag{24}$$

In addition to knowledge of velocity, temperature, and humidity profiles, turbulent kinetic energy and dissipation profiles at the inlet are required for application of the k–ε turbulence model. The eddy viscosity, K_m, and eddy diffusivity of heat, K_h, can be related to the ϕ functions as follows:

$$K_m = \frac{\kappa z u_*}{\phi_m} \tag{25}$$

$$K_h = \frac{\kappa z u_*}{\phi_h} \tag{26}$$

The relation of the eddy diffusivity in the k–ε model will be given in Section 3.

Han et al. [11] compared turbulent kinetic energy and dissipation rate profiles based upon the Monin–Obukhov similarity and mixed layer similarity theories to experimental data for different stability conditions. The mixed layer theory applies to regions outside the surface layer. They found good agreement for turbulent kinetic energy, but over prediction for dissipation rate. The predicted dissipation rate followed the data trend indicating that an appropriate factor would adjust the predicted values to match the measured values. For conciseness, only the relations for the stable regime are provided in (27) and (28), which are piecewise and require smoothing functions. The relations for unstable conditions can be found in references [11,12]. For regions above the PBL, k and ε can be assumed to be zero.

For stable boundary layers ($z/L \geq 0$):

$$\left.\begin{aligned} k &= 6u_*^2 \\ \varepsilon &= \frac{u_*^3}{\kappa z}\left(1.24 + 4.3\frac{z}{L}\right) \end{aligned}\right\}, \quad z \leq 0.1h \tag{27}$$

$$\left.\begin{aligned} k &= 6u_*^2\left(1 - \frac{z}{h}\right)^{1.75} \\ \varepsilon &= \frac{u_*^3}{\kappa z}\left(1.24 + 4.3\frac{z}{L}\right)\left(1 - 0.85\frac{z}{h}\right)^{1.5} \end{aligned}\right\}, \quad z > 0.1h \tag{28}$$

Another method used to represent velocity profiles for different stability classes is the power law relation which has been found to fit data reasonably well in the lower PBL, though not as accurately as the similarity theories. Although it has no theoretical basis, it is mentioned here because it is commonly used and appears as the default option in some available CFD codes. It is of the form

$$\frac{U}{U_r} = \left(\frac{z}{z_r}\right)^p \tag{29}$$

where U_r is the velocity at a reference height, z_r, typically chosen as 10 m. The exponent, p, is a function of z_o, d, stability class, and the height range over which the power law is fitted. If no data are available for a particular site, typical recommended values of p range from 0.15 for an unstable atmospheric condition in an urban area to 0.55 for a stable condition in a rural area. The exponent can be determined from velocity measurements at two different heights as

$$p = \frac{\ln u_2 - \ln u_1}{\ln z_2 - \ln z_1} \tag{30}$$

Or p can be related to the Monin–Obukhov similarity functions by

$$p = \frac{\phi_m(z_r/L)}{\ln(z_r/z_o) - \psi(z_r/L)} \tag{31}$$

where the functions ϕ_m and ψ_m are evaluated at z_r/L instead of z/L.

There is also another approach to arrive at inlet values beyond using the aforementioned similarity functions, however it is more time consuming. The approach involves first performing a 1-D simulation to obtain velocity, temperature, k, and ε profiles, then using these results for boundary and initial conditions for a 3-D simulation. For the 1-D simulation, wind velocity is prescribed at the top boundary and a zero velocity at the bottom. A temperature or heat flux is prescribed at the bottom to represent the chosen stability condition. The values of k and ε at the bottom boundary can be derived from Eqs. (27) and (28). This is the sequence of steps taken by Scargiali et al. for a CFD simulation of heavy gas dispersion over complex terrain [13]. Bear in mind that the results obtained from the 1-D simulation should agree qualitatively to those provided in Section 3, however, quantitatively there might be some variation in magnitude (±20%) due to the uncertainty of the coefficients of the Monin–Obuhkov relations as previously mentioned.

3. The k–ε turbulence model

The k–ε turbulence model [14], based on the Reynolds Averaged Navier–Stokes (RANS) equations, is the most validated and commonly used model for engineering applications. It has performed well for many industrial applications involving confined flows [15]. Its weakness is modeling flows with strong curvature and stagnation points, though variations of this model have been developed to overcome this weakness such as the RNG k–ε turbulence model. Further modifications have been made for buoyancy driven and high shear flows. It should be pointed out that no universal turbulence model exists that can be applied to all applications. Different models may perform better for certain applications than others, and usually within a limited parametric range. Thus, a CFD user should understand a model's limitations by reviewing the literature on model performance, as well as performing validation and parametric sensitivity studies. In this way, a user will have an understanding of the model's range of applicability.

As with all turbulence models, the k–ε model is an approximation to the Navier–Stokes (N–S) equations and as such requires empirically determined coefficients and empirically based assumptions and approximations for the modeled terms. This is also true for subgrid turbulence-based models, that is, large eddy simulation. Only direct numerical simulation (DNS) solves the N–S equations and does not require modeling of additional terms that arise due to filtering or averaging. In this respect, turbulence models share the commonality of invoking approximations and empiricisms with integral-based models, however, they differ significantly by degree. The foundation of the equations used for CFD is based upon the full 3-D, N–S equations, and hence a much lower degree of modeling is required than for integral-based models. This may or may not be an advantage. If the modeling is done poorly, CFD may perform worse than integral-based models. Thus, the process of verification and validation is essential. Given that appropriate verification and validation procedures are performed, CFD-based models can be expected to provide a higher level of accuracy and predictive capability than integral-based models due to the more fundamental nature of their equations [16,17]. They also offer

the advantage of modeling flow fields which include complex terrain and obstacles [18].

The standard k–ε model transport equations for k, the turbulent kinetic energy, and, ε, the turbulence dissipation rate, with the effect of buoyancy included are the following [15]. Overbars and tildes indicate Reynolds-averaged quantities.

$$\frac{\partial(\bar{\rho}k)}{\partial t} + \frac{\partial(\rho\tilde{u}_j k)}{\partial x_j} = \frac{\partial}{\partial x_j}\left(\frac{\mu_t}{\sigma_k}\frac{\partial k}{\partial x_j}\right) + P_k + G_k - \bar{\rho}\varepsilon \tag{32}$$

$$\frac{\partial(\bar{\rho}\varepsilon)}{\partial t} + \frac{\partial(\bar{\rho}\tilde{u}_j\varepsilon)}{\partial x_j} = \frac{\partial}{\partial x_j}\left(\frac{\mu_t}{\sigma_\varepsilon}\frac{\partial \varepsilon}{\partial x_j}\right) + \frac{\varepsilon}{k}(C_{\varepsilon_1}P_k + C_{\varepsilon_1}C_{\varepsilon_3}G_k - C_{\varepsilon_2}\varepsilon) \tag{33}$$

where

$$P_k = \mu_t\left(\frac{\partial\tilde{u}_i}{\partial x_j} + \frac{\partial\tilde{u}_j}{\partial x_i}\right)\frac{\partial\tilde{u}_i}{\partial x_j} - \frac{2}{3}\left(\bar{\rho}k + \mu_t\frac{\partial\tilde{u}_k}{\partial x_k}\right)\frac{\partial\tilde{u}_m}{\partial x_m} \tag{34}$$

$$\mu_t = C_\mu\bar{\rho}\frac{k^2}{\varepsilon} \tag{35}$$

$$C_\mu = 0.09, \quad \sigma_k = 1.0, \quad C_{\varepsilon_1} = 1.44, \quad C_{\varepsilon_2} = 1.92 \tag{36}$$

The turbulent eddy viscosity or diffusivity, μ_t, is not a flow property but will vary depending on the state of turbulence. It can be determined by the product of a velocity ($k^{1/2}$), and length scale ($k^{3/2}/\varepsilon$), computed at each point in the flow by solving the transport equations for k and ε. The term, G_k, accounts for turbulence production or suppression through buoyancy. There have been various formulations for this term, with the most common based on the Boussinesq approximation [15].

$$G_k = \frac{\mu_t}{\bar{\rho}\sigma_k}\beta g_j\frac{\partial\tilde{T}}{\partial x_j} \tag{37}$$

where $\beta = 1/T$ is the thermal expansion coefficient. Various values have been used for C_{ε_3}, ranging from -0.8 for unstable conditions to 2.15 for stable conditions.

The k–ε model has been successfully used for atmospheric flows but requires modification of the form or values of the coefficients [19–23]. Richards and Hoxey [23] showed that for neutral conditions, and assuming the similarity relations from the Monin–Obuhkov theory, these coefficients should be of the form

$$C_\mu = \frac{u_*^4}{k^2}, \qquad \sigma_\varepsilon = \frac{\kappa^2}{(C_{\varepsilon_2} - C_{\varepsilon_1})\sqrt{C_\mu}} \tag{38}$$

Recently, Alinot and Masson [19] modified the k–ε model in the commercially available code, FLUENT, for unstable, neutral, and stable conditions. With modifications to the coefficients, their model was able to reproduce the Monin–Obukhov profiles. While it has been demonstrated that modifications are required for the k–ε model to reproduce representative profiles in the surface layer, the question of what effect error in profile representation has on LNG dispersion remains to be answered. There is reason to believe that errors in profile representation by not modifying the k–ε model are not significant though investigation of this would still be beneficial. Sklavounos and Rigas [24] compared simulation results using the commercially available code, CFX, to the experimental results from the Coyote LNG series trials [25–27]. They found good agreement for concentration values, with a geometric mean bias of about 0.9 with a slight tendency to overpredict, for tests performed in unstable and stable conditions without modification to the standard k–ε model. The simulation results were well within a factor of 2 from the experimental results. However, these results pertain to the surface layer and to flows which are not affected by the Coriolis force.

Due to the motion of the Earth, the laws of motion for atmospheric flows are in an accelerating frame of reference. Thus, the momentum equations must be modified by the addition of the Coriolis and centrifugal forces. These forces are always present since the frame of reference is Earth's surface, but they may be neglected if other forces dominate, such as inertial and frictional. The non-dimensional parameters, the Rossby and Ekman numbers, are used to compare these inertial and frictional forces to that of the Coriolis force.

$$\text{Rossby number} = \frac{\text{inertial force}}{\text{Coriolis force}} = \frac{V}{Df} \tag{39}$$

$$\text{Ekman number} = \frac{\text{frictional force}}{\text{Coriolis force}} = \frac{\nu}{D^2 f} \tag{40}$$

where V, D, f, and ν are a characteristic velocity, characteristic length, Coriolis parameter, and kinematic viscosity, respectively.

Since inertial forces typically dominate in atmospheric flows, the Rossby number (Ro) is used to determine whether the Coriolis force should be included. Small Ro numbers indicate that the Coriolis force must be included in the equations of motion. For ocean circulations, the Rossby number is about 5×10^{-3} with $D \sim 3000$ km, $V \sim 1.5$ m/s, and $f \sim 10^{-4}$ s^{-1}, while for bathtub vortices $Ro \approx 10^5$, with $D \sim 1$ cm, $V \sim 0.1$ m/s, and $f \sim 10^{-4}$ s^{-1} [25]. At the equator the Coriolis force can be neglected since $f = 0$ there.

Within the surface and mixed layer, frictional forces become important and under the influence of the Coriolis force the boundary layer becomes twisted. If the axis of rotation within the boundary layer is perpendicular to the surface, the boundary layer is termed the Ekman layer, if parallel to the surface it is termed the Stewartson layer [28]. The flow trajectory is deflected and additional shear is introduced due to the turning of the velocity vector with height within the layer. This turning has been found to be approximately 30° or more between the surface and the top of the boundary layer (up to 300 m) for a stable atmosphere [29]. This effect is called the Ekman spiral. Thus, the velocity field is no longer two dimensional as in the surface layer, but has a non-zero V_g component (horizontal y-direction) to the velocity vector.

The question arises as to whether the Coriolis force can be neglected for LNG spill volumes up to 300,000 m^3, pertaining to spills over water. If the wind speed is 2 m/s, $f \approx 10^{-4}$ s^{-1}, and D, chosen as the greatest dimension ($\sim$10 km) of the NG cloud, then the Ro number is about 2, which indicates that the Coriolis

and inertial force are both important. Currently, there has been no simulation that has included both the Coriolis force and the dynamics of LNG dense-gas dispersion. Thus, this is an area in need of further investigation. The main question is: what is the effective magnitude of the Coriolis force on the trajectory and maximum distance to the LFL of the NG cloud?

With the Coriolis force included, the Reynolds-averaged momentum equations are the following:

$$\frac{\mathrm{D}\tilde{u}}{\mathrm{D}t} = f\tilde{v} - \frac{1}{\rho}\frac{\partial p}{\partial x} + \nu\nabla^2\tilde{u} - R_\mathrm{s} \tag{41}$$

$$\frac{\mathrm{D}\tilde{v}}{\mathrm{D}t} = -f\tilde{u} - \frac{1}{\rho}\frac{\partial p}{\partial y} + \nu\nabla^2\tilde{v} - R_\mathrm{s} \tag{42}$$

$$\frac{\mathrm{D}\tilde{w}}{\mathrm{D}t} = -\frac{1}{\rho}\frac{\partial p}{\partial z} + g + \nu\nabla^2\tilde{w} - R_\mathrm{s} \tag{43}$$

where R_s is the Reynolds-stress tensor and is modeled using the Boussinesq hypothesis by

$$R_\mathrm{s} = \frac{\partial}{\partial x_j}\left[\mu_\mathrm{t}\left(\frac{\partial\tilde{u}_i}{\partial x_j} + \frac{\partial\tilde{u}_j}{\partial x_i}\right) - \frac{2}{3}\frac{\partial\tilde{u}_k}{\partial x_k}\delta_{ij}\right] \tag{44}$$

For unstable and stable conditions under the influence of the Coriolis force it has been found that the k–ε model requires additional modification to the ε-equation [30–35]. The standard model tends to over predict the boundary layer depth and turbulent mixing [34,35].

4. Simulation specifications

When using a CFD code, usually there are several options available for boundary conditions and a user must decide what boundary conditions are most appropriate for their application. Initial conditions must also be decided, as well as the size of the domain and the grid. The following addresses these issues by providing a general description and discussion on the boundary conditions, initial conditions, as well as domain and grid determination appropriate for LNG dispersion. The objective of the following is to point out particular features that a code user should be aware of with the assumption that the user has basic knowledge of condition, domain, and grid application. Detailed discussion and description of these can be found in [36,37].

4.1. Boundary conditions

Typically, there are seven boundary conditions required for an LNG simulation: the inlet, outlet, top, two sides, and bottom of the computational domain, and additionally the LNG pool itself as shown in Fig. 1.

4.1.1. Inlet

The inlet boundary conditions for the computational domain are specified by a Dirichlet condition, that is, the values of the variables on the boundaries are given. For the k–ε model, this requires that all components of velocity, k, and ε are provided. A reference pressure of zero is typically assumed at the inlet. In addition, temperature and concentration values are required for LNG dispersion. The components of velocity, k, ε, and temperature can be specified from the relations provided in Section 2 or by those obtained from a 1-D simulation as previously mentioned. Typically, air is the default species and is provided without explicit specification. Otherwise, concentration of oxygen and nitrogen must be specified. The concentration of methane would of course be zero at the inlet boundary of the computational domain.

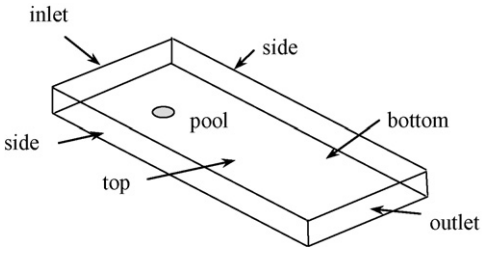

Fig. 1. Boundaries of computational domain.

4.1.2. Outlet

The outlet boundary of the computational domain is prescribed by specifying zero normal gradients for all variables, except pressure. Alternatively, a constant pressure can be specified at the outlet and mass fluxes calculated through the continuity equation and extrapolation. All other variables are extrapolated as well. This method is preferred when little information is known about the flow variables except pressure, and is typically used for external flows. In some available codes this boundary condition is termed ‘open’, ‘outlet’, or ‘outflow’. This condition assumes that the flow is fully developed, unidirectional and variables are not changing in the flow direction. Thus, it is important to place this boundary far from the NG cloud otherwise significant errors can propagate throughout the domain if this boundary condition is not satisfied. Placement of boundaries will be further discussed in the section addressing domain size.

4.1.3. Top

The top boundary is an external flow boundary. It would seem that an ‘open’ flow condition would apply in which the pressure is specified as described under the outlet condition. However, the application of this condition will significantly alter the specified inlet flow profile since the prescribed pressure may not provide the desired velocity value at the top boundary. It would also seem that a velocity compatible with the inlet velocity profile should be specified, but this will be incompatible with the wind profile once it is altered by the release of the NG vapors.

Ideally, the NG vapors should be injected into a flow field that has a velocity profile representative of the relations given in Section 2. A slip or symmetry boundary condition along the top plane will allow for this. A slip boundary condition sets the boundary velocity as equal to the fluid velocity. This is equivalent to a symmetry condition in which no flow crosses the top boundary and there is no scalar flux across the top boundary. Thus, the normal component of velocity is set to zero and all other variables have boundary values set equal to the flow value.

The top boundary must be placed sufficiently far away so that this boundary condition is not violated.

4.1.4. Sides

It would seem that an open boundary condition would be appropriate for the side external flow boundaries, but for reasons provided in Section 4.1.3 the desired velocity profile will be significantly altered since pressure or alternatively zero normal velocity gradients are prescribed. Excessive mixing will be introduced into the domain, enough to result in a significant decrease in the distance to LFL. The appropriate boundary condition to apply is symmetry as described in Section 4.1.3 with the side boundaries placed sufficiently far away in order not to violate this boundary condition.

4.1.5. Bottom

The bottom boundary condition is specified with a no-slip condition in which all velocity components are zero. The other variables are set according to wall functions which avoid the need to resolve the turbulent boundary layer near the wall. These wall functions are based on the universal behavior of flows near walls. Detailed description of these functions can be found in references [33,34]. The different stability conditions discussed in Section 2 can be modeled by specifying a temperature or heat flux at the bottom boundary where negative fluxes correspond to stable conditions and positive fluxes correspond to unstable conditions. A concentration flux value for water vapor can also be prescribed at this boundary to model humidity levels.

4.1.6. Pool

The dynamics of the pool are extremely complex particularly for spills over water where waves and currents can affect pool spreading. Under these conditions the LNG spreads on a turbulent interface and the pool thickness will be very thin (∼1 cm). Trying to resolve this thin turbulent layer within an LNG dispersion simulation is computational cost prohibitive. An alternative approach would be to perform a calculation of just the pool using a free-surface code. Then the information on pool spread and evaporation obtained from this simulation can be used as input for the NG cloud simulation. To date, there are no free-surface codes that have the capability to perform such a calculation, but development is possible if experimental data, not currently available, was obtained. There is also the occurrence of rapid phase transition (RPT) explosions due to the temperature difference between the LNG and water resulting in explosive boiling. These RPTs occur infrequently during an LNG spill and affect dispersion by creating large puffs of gas, increasing the distance to the LFL as found from experiment [25–27].

Due to the difficulties of modeling such complexities, the approach to modeling the pool is to assume a circular shape and to prescribe an inlet velocity. The pool diameter is determined by a mass balance between the LNG source and the pool evaporation. The inlet pool velocity for use in a simulation is in the gas phase, thus it is determined by

$$v_g = \frac{(\rho v)_{liq}}{\rho_g} \tag{45}$$

where ρ_g is the NG density ($\approx$1.76 kg/m^3 at 111 K) and $(\rho v)_{liq}$ is the mass flux of LNG. Experimental values for the LNG pool mass flux range from 0.029 to 0.195 kg/(m^2 s). Due to the range of measured values and measurement uncertainty several simulations should be performed to ascertain the effect of the inlet pool velocity on dispersion distances. Keep in mind that changing the mass flux of the NG vapors will change the diameter of the pool.

The values of k and ε above the pool surface can be approximated with the length scale, D, in this case the pool diameter and a turbulent intensity, T_i (∼1–10%).

$$k = \tfrac{3}{2}(v_g T_i)^2 \tag{46}$$

$$\varepsilon = C_\mu^{3/4} \frac{k^{3/2}}{0.07D} \tag{47}$$

The turbulent intensity is not known exactly so a sensitivity analysis can be performed to ascertain the effective magnitude of this value on the results.

The temperature of the LNG pool (111 K) must also be specified and is very important since its temperature difference from the surroundings is responsible for dense-gas behavior. The water or ground surface temperature or heat flux must also be specified.

4.2. Initial conditions

All variables must be given initial values. Ideally, the flow field should be uniformly initialized with the inlet conditions. If this is not possible, then it is necessary to initialize all variables to zero and allow the flow field to fully develop before releasing the vapors. Some codes do not allow for very much flexibility in initialization, a uniform value in space being the only option. One might expect that initializing the flow field with a uniform value other than zero may expedite the time required to reach a developed flow field. This should be avoided since it can result in extreme artificial mixing because the inlet velocity values will be entering a domain where the initialized velocity values will be greater and some lower than the inlet values thereby resulting in opposing pressure gradients.

4.3. Domain and grid

The approach to determining an adequately sized domain is to perform exploratory simulations for different domain sizes. This can be done using a coarse mesh. The methane concentration contours over time can be monitored to see if there are boundary effects. The 5 and 2.5% volume concentration levels are typically of interest because the k–ε model is based upon a time-averaged formulation and the 'true' LFL may be between the 2.5 and 5% simulated concentration levels. Thus, the maximum distances to the 2.5 and 5% concentration levels should be reported with the realization that the actual distance to a 5% concentration is somewhere in between. When these concentration contours do not change significantly (<1% change) a sufficient domain size is reached based on a coarse mesh. It can be expected that using a finer mesh will result in a shorter distance to LFL since turbulent

mixing is better resolved. Hence, the domain determined using a coarse mesh should be adequate.

A stretched grid in the vertical direction in which nodal points are concentrated in the cloud region near the surface should be used due to the size of the domain and the relatively short height of the cloud. Evenly spaced nodal points based on spacing necessary to resolve the cloud vertically would be computational cost prohibitive. For the horizontal direction the grid is more uniform due the extent of the cloud, although a slightly stretched grid may be used in which nodal points are somewhat concentrated in regions of the cloud. This can be ascertained in an approximate way by the exploratory simulations performed for domain determination.

The number of nodal points required to adequately resolve the cloud can be determined by performing a grid study. Successive grids, at least three, differing by a factor of 2 can be tested to determine grid affects on the solution. Due to the extent of these clouds and the number of nodes required, a grid independent solution usually cannot be reached. Thus, an estimate of the exact solution can be determined from using Richardson's extrapolation. By determining discretization error from solutions on successive grids an estimate of the exact solution can be determined. When the solution displays monotonic behavior this method is fairly accurate. A detailed description of Richardson's extrapolation can be found in [37].

5. Validation datasets

During the late 1970s and the 1980s a number of large LNG spill experiments were conducted at China Lake in California, Maplin Sands in the United Kingdom, and the Nevada Test Site. The goal of all of these experiments was to measure the evaporation, dispersion, and combustion of spilled LNG so intensively that the datasets produced could be used as benchmarks for the validation of computer models of that time and in the future. To do that required extensive measurements of meteorological parameters such as wind speed, temperature, turbulence, humidity and solar heat flux, and gas cloud parameters such as concentration, temperature, and ground heat flux, over an extensive area and at various heights. It was necessary to conduct the tests under a variety of meteorological and environmental conditions that would include all those that might be encountered in a real incident. A summary of LNG tests and their characteristics is given in another paper in this journal. From these tests, the best were selected to be benchmark tests for dispersion model validation. These include: Burro 3, 7, 8, 9, Coyote 3, 5, 6, Falcon 1, 3, 4, and Maplin (Shell) 15, 27, 29, 34, 35, 39, 56. A summary of these tests, except for Falcon, was developed by Ermak et al. [38] specifically for model validation and includes key parameters required to run the models for each test, such as the Monin–Obukhov parameters, roughness lengths, humidity, LNG composition, spill rate, etc. Information on Falcon can be obtained from the Falcon Data Report [39] and from an analysis paper by Chan [40]. Burro information is available from the Burro Data Report [9] and from several analysis papers [41,42] and Coyote information from the Coyote Data Report [25,26] and several analysis papers [27,41].

The most important tests in all of the test series are Burro 8 and Falcon 1, because they were conducted under low wind speed and stable atmospheric conditions. Burro 8 and Falcon 1 were the only tests to show clearly the effects of large dense vapor clouds excluding atmospheric turbulence and dominating atmospheric dispersion. Since Falcon 1 was done for vapor fence evaluation and not free field dispersion, it is less valuable for model validation, leaving only Burro 8 available for clearly demonstrating dense-gas effects on dispersion in open terrain. The average Burro 8 wind speed was 1.8 m/s but it presents a modeling challenge because the wind speed dropped steadily during the test. Gravity flow of the vapor cloud caused Burro 8 to form the widest and lowest cloud of any of the Burro and Coyote tests and produced the highest peak concentrations and longest distance to the LFL (445 m) of any of these tests. The modest China Lake terrain had a significant effect on the Burro 8 cloud because of the low wind speed and stable atmosphere. Burro 8 involved the lowest level of ambient turbulence of any of these tests allowing the turbulence within the cloud to be damped by the dense gas. These effects are discussed in more detail in Morgan [41], Chan [43], Chan and coworkers [44] and Ermak and coworkers [45]. Burro 9 had the highest spill rate of all the Burro and Coyote tests (18.4 m^3/min), a moderate wind speed (5.7 m/s), neutral stability and makes an excellent validation test case example. It had the longest LFL distance, 270 m neglecting RPTs, of all but Burro 8.

Each measurement has an associated uncertainty and those are best obtained from the data reports and the analysis reports. Assessing the uncertainty in a derived parameter is more difficult because of the need to include the variable contributions of wind, water, sun, and other environmental parameters. Burro 7 had the largest spill volume, 39.4 m^3, of all the Burro and Coyote tests and its spill duration of 174 s was among the longest. Because of the long duration of this spill, it provides a good example of steady state characteristics. When the vaporization rate equals the spill rate and the LFL has reached its furthest distance downwind, the vapor cloud is said to be in steady state. For this test, steady state existed from about 40 to 190 s at 140 m downwind, with concentrations varying from 3 to 7% during this time with a mean of about 5%. Since plume meander can only lower the concentration below the maximum value, the steady state concentration was greater than 5%. According to the analysis of Morgan et al. [41] this implies an uncertainty of about ±15% in concentration and also implies an uncertainty of ±15% in LFL distance. We assume that this is typical of all of the tests at steady state.

Each measurement also has a characteristic response time associated with it, as do the computer models. The field tests employed instruments with varying response times. Data from turbulence measuring stations were sampled at 0.2 and 0.3 s. Gas concentration measuring stations were sampled at 1 s intervals. Gas concentration data from fast gas sensors were averaged over 10 s and combined with data from slower sensors for contour generation and used for determining LFL distances. Examination of the Coyote gas concentration data using a 2 s average rather than the nominal 10 s average, resulted in increased peak concentrations, reflecting the random nature of the fluctuations.

Sample calculations gave differences in the LFL distances that were less than the experimental uncertainty of 15% [41].

6. Model validation

Model validation involves detailed comparison of model calculations with benchmark test data. This does not mean comparison of a single parameter, such as the LFL but rather comparison of all important parameters that influence dispersion of the vapor cloud. Particular care is needed for LNG spill predictions because the spills of interest are typically several orders of magnitude larger than any experimental data available for model validation. In order to have confidence that these models are making accurate predictions orders of magnitude beyond their validation datasets, it must be assured that all of the physics and chemistry important at the larger scale is correctly modeled. Thus, particularly for LNG, it is important to compare multiple parameters with test data, ideally at several scales. With LNG dispersion, temperature is particularly important since temperature changes the buoyancy and consequently the dispersion behavior of the LNG vapor cloud. For model validation, it is desirable to make temperature comparisons at various downwind distances as close to cloud centerline as possible and to look for systematic deviation between model and data. Note that when comparing simulation results to the Burro and Coyote data that the sensor locations are specified relative to a coordinate system that is not aligned with the wind direction. Since a simulation typically has a coordinate system aligned with the wind direction a rotation transformation is required to compare the same locations. In the Burro and Coyote tests, the x-coordinate was defined to be in the downwind direction and y-coordinates in the crosswind direction. Thus, if X_1 and Y_1 are the given coordinates in the test reports then to transform to X_2 and Y_2, the simulation locations relative to the wind, the following relations can be used:

$$X_2 = X_1 \cos\theta + Y_1 \sin\theta \tag{48}$$

$$Y_2 = Y_1 \cos\theta - X_1 \sin\theta \tag{49}$$

During the Burro 8 test the wind direction was shifted 9.8° from the sensor array coordinate system, thus the transformed location for sensor G11 at the 140 m arc, as an example, would be the following as shown in Table 1. The transformed coordinates differ significantly, indicating the importance of performing this transformation in order to compare corresponding locations between simulation and data measurements.

Several examples of these comparisons have been selected from the available experimental datasets and published CFD results. In Fig. 2, we see temperature data from Burro 8 measurements at 1 m elevation for 57 and 140 m downwind, compared to FEM3 CFD calculations, with and without China Lake terrain effects, from Morgan et al. [41]. It is clear that terrain effects are important for Burro 8 calculations. The model under estimates the initial temperature drop when terrain effects are included at 57 m but is better at 140 m. The model has the temperature returning to ambient too quickly at both locations, probably because it does not account for the fact that the ground cools, thereby reducing the heat flow, nor for the fact that the wind speed decreases steadily during the test.

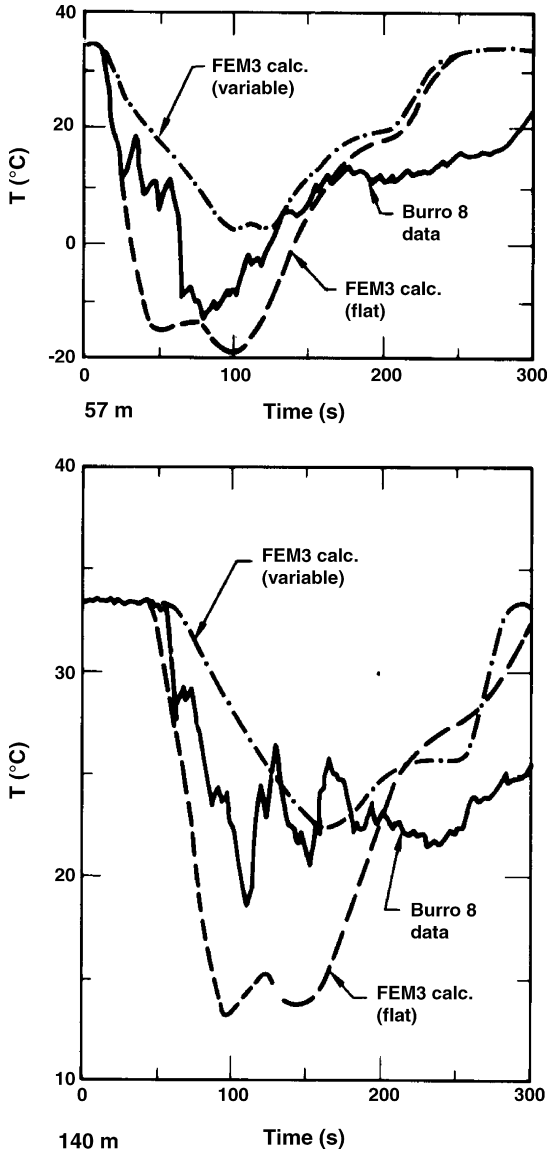

Fig. 2. Comparison of Burro 8 temperature measurements at 1 m elevation at 57 and 140 m downwind, with FEM3 calculations with the China Lake terrain and with flat terrain. Taken from Morgan [41].

Table 1
Example of coordinate transformation for Burro 8 data

Sensor (at 140 m arc)	x-Location (m) (relative to sensor array centerline)	y-Location (m) (relative to sensor array centerline)	Rotation angle (rad)	x-Location (m) (relative to wind direction)	y-Location (m) (relative to wind direction)
G11	112	−84	0.171	96.1	−101.8

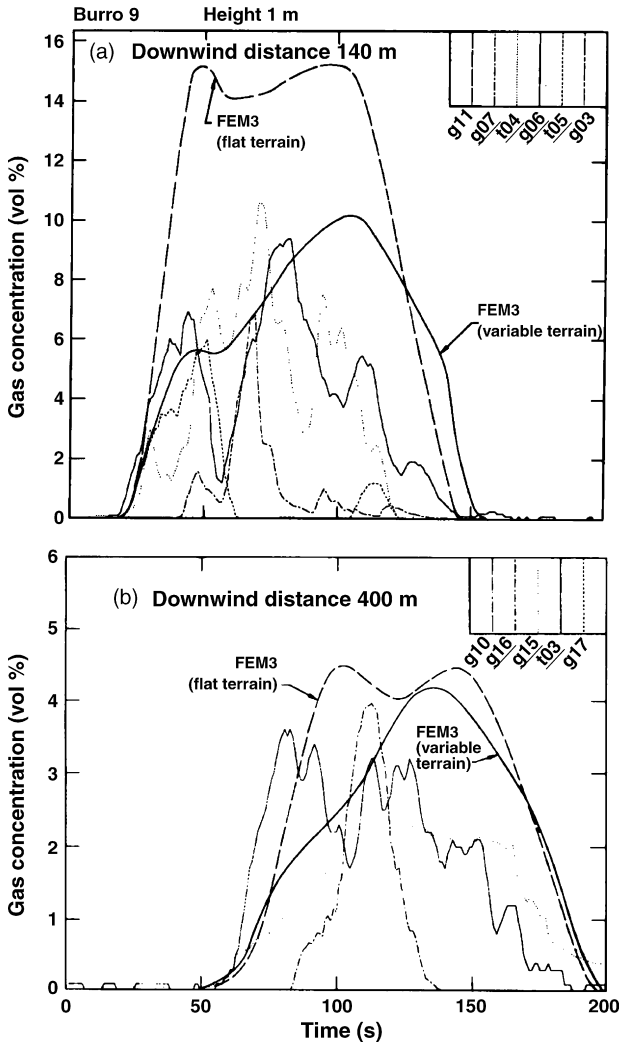

Fig. 3. Burro 9 gas concentration measurements at 1 m elevation at 140 and 400 m down wind, compared to FEM3 calculations with and without China Lake terrain. Taken from Morgan [41].

Gas concentration is ultimately the parameter of most interest. Here too it is desirable to compare model calculations with data for various distances downwind and to look for trends as a function of downwind distance that indicate systematic deviation between model and data. As an example, Fig. 3 shows a comparison of Burro 9 gas concentration data at the 1 m elevation for 140 and 400 m downwind with FEM3 calculations with China Lake terrain and with flat terrain [41]. The multiple data curves on each figure are concentration measurements taken along the specified arc. Clearly even the modest China Lake terrain effects are important for this test as well as Burro 8. Probably the most valuable comparisons for model validation are gas concentration plume parameters. The four recommended by Ermak et al. [38] are maximum gas concentration, average ground-level plume centerline concentration, plume half-width and plume height, all as a function of downwind distance. In Fig. 4 from Morgan et al. [41] the Burro 9 gas concentration contours generated from gas concentration data are compared to calculated contours at 1 m above ground at the time of maximum extent. At 80 s and within about 100 m of the source, the

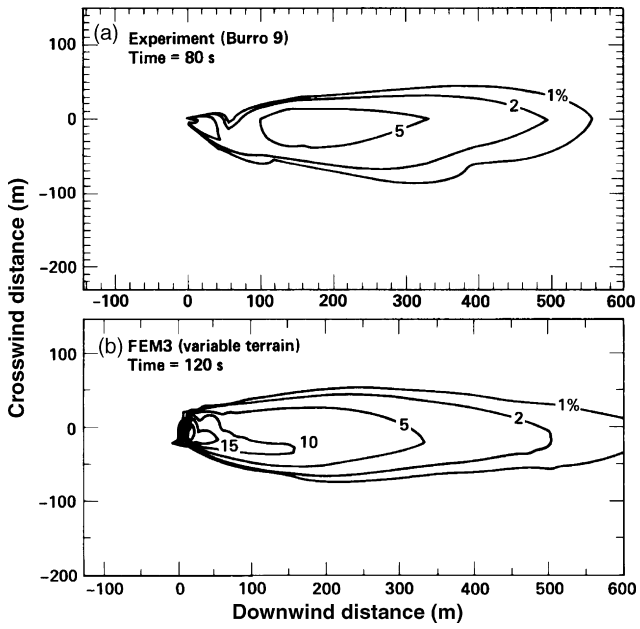

Fig. 4. Comparison of Burro 9 horizontal contours at 1 m elevation with FEM3 calculations which include China Lake terrain. Taken from Morgan [41].

experimental contours are not very reliable because the sensors close to the spill point were covered by mud from the RPTs. The difference in time may be due to variations in ambient wind speed, variations in vapor generation rate or the large RPTs that occurred late in the test and perturbed the vapor cloud. Fig. 5 shows a comparison of the Burro 9 peak concentrations as a function of downwind distance with FEM3 calculations on a log–log plot [41]. Corrections are made for terrain effects and for RPT effects. It is apparent that RPTs increased the peak concentrations downwind, although only for a very brief time. Crosswind

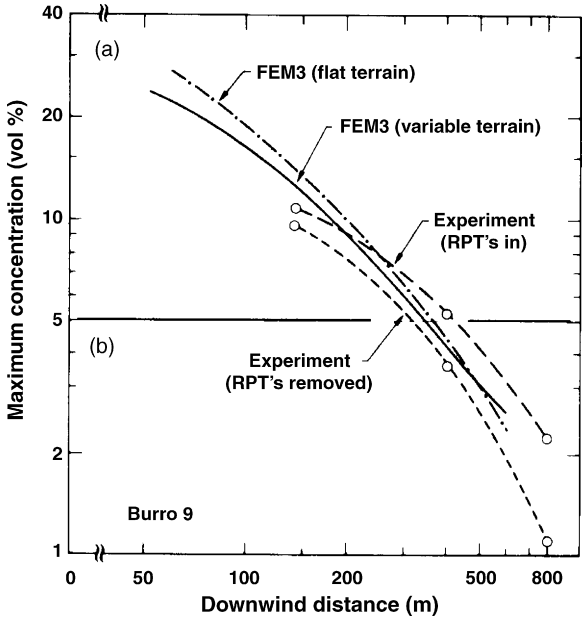

Fig. 5. Peak Burro 9 gas concentration data with and without RPT influence removed vs. downwind distance compared to FEM3 calculations with and without China Lake terrain included. Taken from Morgan [41].

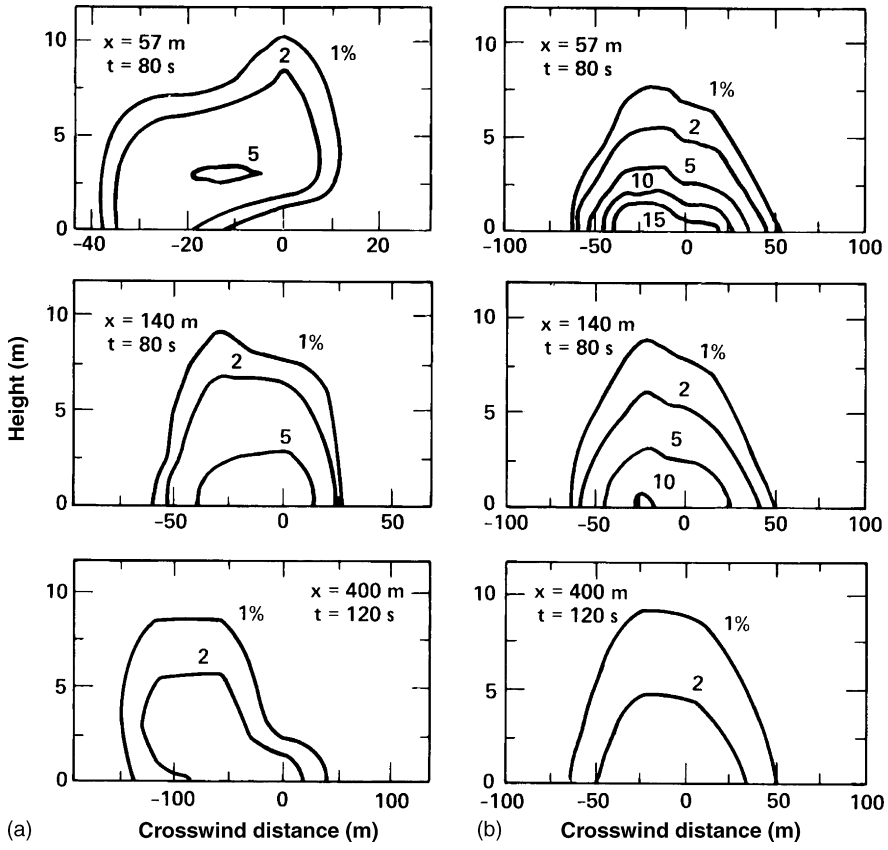

Fig. 6. Burro 9 vertical vapor concentration (vol%) contours, crosswind at various downwind distances and selected times compared to FEM3 calculations. Note different horizontal scales. Taken from Morgan [41]. (a) Experiment (Burro 9) and (b) FEM3 (variable terrain).

gas concentration comparisons at multiple downwind distances are also important for model validation. Fig. 6 shows crosswind contours for Burro 9 at downwind distances of 57, 140, and 400 m compared to FEM3 calculations that included China Lake terrain [41]. The times were chosen during the steady state phase of vapor cloud development when the cloud achieved maximum crosswind extent. The FEM3 calculations agree well with the experimental contours, except at 57 m downwind where the low experimental values are due to mud splattered on the gas sensors by RPTs.

7. Conclusion

The primary intent of this paper was to provide a CFD user with an understanding of first-order effects on simulated LNG vapor dispersion distances, and to bring forth issues that a user should be aware of before attempting a simulation. As previously noted, it is important for a CFD code to model the level of turbulent mixing in the atmosphere. Thus, the pre-LNG release simulated profiles of velocity, temperature, turbulent kinetic energy, and dissipation must be compared against either measured profiles or approximate functions based on similarity theories.

It is also imperative that simulation results are compared with experimental data such as those available from the Burro, Coyote, and Falcon tests. As previously stated, there is no universal turbulence model and thus a user must realize the range of applicability of the model under use. This can be done by researching relevant literature, and more importantly performing a sensitivity analysis by varying parameters such as the inlet pool velocity and atmospheric profiles to determine their effect on dispersion distances. Sensitivity to atmospheric profiles alludes not only to different stability conditions, but also to measurement uncertainty. Given that measurement uncertainty can vary by typically $\pm 20\%$, sensitivity to this variation should be performed. It would also be of interest to test a code not only with magnitude variation but also the shape or form of the functional relations specified in Section 2.

Designing a computational experiment includes specifying the domain, grid, boundary and initial conditions. To arrive at a final result a user must go through an iterative process, such as that involved in appropriate domain and grid determination which usually cannot be arrived at from a first attempt. Each of these specifications can have a very significant effect on dispersion distances. It is recommended that a user experiment with variation of these specifications to realize the magnitude of their effect.

Finally, an additional physical consideration raised in this paper is the inclusion of the Coriolis force. Given the possible scale of releases from currently proposed offshore facilities, the effect of this force on LNG dispersion should be ascertained. It is a question of not only determining how much additional

mixing is introduced due to the Ekman boundary layer, but also the degree to which it changes the cloud trajectory.

Acknowledgements

The authors would like to thank the following individuals for their review and valuable discussion of the manuscript: T. Blanchat, T.Y. Chu, and V. Nicolette. Sandia is a multiprogram laboratory operated by Sandia Corporation, a Lockheed Martin Company, for the United Stated Department of Energy under Contract DE-AC04-94AL85000.

References

[1] S.P. Arya, Micrometeorology and atmospheric boundary layer, Pure Appl. Geophys. 162 (2005) 1721–1745.
[2] U. Hogstrom, Review of some basic characteristics of the atmospheric surface layer, Boundary-Layer Meteorol. 78 (1996) 215–246.
[3] H.A. Panofsky, The atmospheric boundary layer below 150 meters, Annu. Rev. Fluid Mech. 6 (1974) 147–177.
[4] S.R. Hanna, R. Britter, Wind Flow and Vapor Dispersion at Industrial and Urban Sites, Center for Chemical Process Safety/AIChE, 2002.
[5] H.A. Panofsky, J.A. Dutton, Atmospheric Turbulence: Models and Methods for Engineering Applications, John Wiley & Sons, Inc., Canada, 1984.
[6] S.P. Arya, Introduction to Micrometeorology, second ed., Academic Press, San Diego, 2001.
[7] D.J. Tritton, Physical Fluid Dynamics, second ed., Oxford University Press, Great Britain, 1988.
[8] F. Pasquill, F.B. Smith, Atmospheric Diffusion, third ed., Elllis Horwood Ltd., West, Sussex, England, 1983.
[9] R.P. Koopman, et al., Burro Series Data Report LLNL/NWC 1980 LNG Spill Tests, Lawrence Livermore National Laboratory, UCID-19075, 1982.
[10] W. Weng, P.A. Taylor, On modelling the one-dimensional atmospheric boundary layer, Boundary-Layer Meteorol. 107 (2003) 371–400.
[11] J. Han, S.P. Arya, S. Shen, Y. Lin, An estimation of turbulent kinetic energy and energy dissipation rate based on atmospheric similarity theory, Report no. NASA/CR-2000-210298, 2000.
[12] S.P. Arya, Atmospheric boundary layers and turbulence, in: Z. Boybeyi (Ed.), Mesoscale Atmospheric Dispersion, WIT Press, Computational Mechanics Publications, 2001.
[13] F. Scargiali, E. Di Rienzo, M. Ciofalo, F. Grisafi, A. Brucato, Heavy gas dispersion modelling over a topographically complex mesoscale: a CFD based approach, Proc. Safety Environ. Protect 83 (B3) (2005) 242–256.
[14] W.P. Jones, B.E. Launder, The prediction of laminarization with a two-equation model of turbulence, Int. J. Heat Mass Transfer 15 (1972) 301–314.
[15] C. Chen, S. Jaw, Fundamental of Turbulence Modeling, Taylor and Francis, Washington, DC, 1987.
[16] B. Carissimo, et al., The SMEDIS database and validation exercise, Int. J. Environ. Pollut. 16 (2001) 614–629.
[17] N.C. Daish, SMEDIS: scientific model evaluation of dense gas dispersion models, Int. J. Environ. Pollut. 14 (1–6) (2000) 39–51.
[18] S. Kim, F. Boysan, Application of CFD to environmental flows, J. Wind Eng. Ind. Aero. 81 (1999) 145–158.
[19] C. Alinot, C. Masson, k–ε model for the atmospheric boundary layer under various thermal stratifications, J. Solar Eng. 127 (November) (2005) 438–443.
[20] A. Huser, P.J. Nilsen, H. Skatun, Applications of k–ε model to the stable ABL: pollution in complex terrain, J. Wind Eng. Ind. Aero. 67–68 (1997) 425–436.
[21] R. Morel, A. Laassibi, E. Alcaraz, R. Zegadi, G. Brun, D. Jeandel, Validation of a k–ε model based on experimental results in a thermally stable stratified turbulent boundary layer, Int. J. Heat Mass Transfer 35 (1992) 2717–2724.
[22] T.W. Abou-Arab, M.A. Serag-Eldin, Turbulence modeling and simulation of atmospheric boundary layers, J. Fluids Eng. 114 (1992) 43–44.
[23] P.J. Richards, R.P. Hoxey, Appropriate boundary conditions for computational wind engineering models using the k–ε turbulence model, J. Wind Eng. Ind. Aero. 46–47 (1993) 145–153.
[24] S. Sklavounos, F. Rigas, Simulation of Coyote series trials—Part I: CFD estimation of non-isothermal LNG releases and comparison with box-model predictions, Chem. Eng. Sci. 61 (2006) 1434–1443.
[25] H.C. Goldwire Jr., H.C. Rodean, R.T. Cederwall, E.J. Kansa, R.P. Koopman, J.W. McClure, T.G. McRae, L.K. Morris, L. Kamppinen, R.D. Kiefer, Coyote Series Data Report LLNL/NWC 1981 LNG Spill Tests Dispersion, Vapor Burn, and Rapid-Phase-Transition, vol. 1, UCID-19953, 1983.
[26] H.C. Goldwire Jr., H.C. Rodean, R.T. Cederwall, E.J. Kansa, R.P. Koopman, J.W. McClure, T.G. McRae, L.K. Morris, L. Kamppinen, R.D. Kiefer, Coyote Series Data Report LLNL/NWC 1981 LNG Spill Tests Dispersion, Vapor Burn, and Rapid-Phase-Transition, vol. 2, Appendices, UCID-19953, 1983.
[27] H.C. Rodean, W.J. Hogan, P.A. Urtiew, H.C. Goldwire Jr., T.G. McRae, D.L. Morgan Jr., Vapor burn analysis for the Coyote series LNG spill experiments, UCRL-53530, 1984.
[28] H.J. Lugt, Vortex Flow in Nature and Technology, John Wiley & Sons, Inc., Canada, 1983.
[29] B. Kosovic, J.A. Curry, A large eddy simulation study of the quasi-steady, stably stratified atmosphere boundary layer, J. Atmos. Sci. 57 (2000) 1052–1068.
[30] F.R. Freedman, M.Z. Jacobson, Modifications of the standard ε-equation for the stable ABL through enforced consistency with Monin–Obukhov similarity theory, Boundary-Layer Meteorol. 106 (2003) 383–410.
[31] D.D. Apsley, I.P. Castro, A limited-length-scale k–ε model for the neutral and stably-stratified atmospheric boundary layer, Boundary-Layer Meteorol. 83 (1997) 75–98.
[32] P.G. Duynkerke, Application of the E–ε turbulence closure model to the neutral and stable atmospheric boundary layer, J. Atmos. Sci. 45 (1988) 865–879.
[33] H. Burchard, O. Petersen, T.P. Rippeth, Comparing the performance of the Mellor–Yamada and the k–ε two-equation turbulence models, J. Geo. Res. 103 (1998) 10,543–10,554.
[34] H.W. Detering, D. Etling, Application of the e–ε turbulence model to the atmospheric boundary layer, Boundary-Layer Meteorol. 33 (1985) 113–133.
[35] J.G. Bartzis, New approaches in two-equation turbulence modelling for atmospheric applications, Boundary-Layer Meteorol. 116 (2005) 445–459.
[36] J.H. Ferziger, M. Peric, Computational Methods for Fluid Dynamics, third ed., Springer, New York, 2002.
[37] H.K. Versteeg, W. Malalasekera, An Introduction to Computational Fluid Dynamics, Addison Wesley Longman Limited, England, 1995.
[38] D.L. Ermak, R. Chapman, H.C. Goldwire, F.J. Gouveia, H.C. Rodean, Heavy Gas Dispersion Test Summary Report, Lawrence Livermore National Laboratory, UCRL-21210, October 1988.
[39] T.C. Brown, et al., Falcon Series Data Report, 1987 LNG Vapor Barrier Verification Field Trials, Lawrence Livermore National Laboratory, UCRL-CR-104316, June 1990.
[40] S.T. Chan, Numerical simulations of LNG vapor dispersion from a fenced storage area, J. Hazard. Mater. 30 (1992) 195–224.
[41] D.L. Morgan, L.K. Morris, S.T. Chan, D.L. Ermak, T.G. McRae, R.T. Cederwall, R.P. Koopman, H.C. Goldwire, J.W. McClure, W.J. Hogan, Phenomenology and Modeling of Liquefied Natural Gas Vapor, Lawrence Livermore National Laboratory, UCRL-53581, April 1984.
[42] R.P. Koopman, R.T. Cederwall, D.L. Ermak, H.C. Goldwire, W.J. Hogan, J.W. McClure, T.G. McRae, D.L. Morgan, H.C. Rodean, J.H. Shinn, Analysis of Burro series 40-m^3 LNG spill experiments, J. Hazard. Mater. 6 (1–2) (1982) 43–83.
[43] S.T. Chan, D.L. Ermak, Recent results in simulating LNG vapor dispersion over variable terrain, in: Proceedings of the IUTAM Symposium on Atmo-

spheric Dispersion of Heavy Gases and Small Particles, Delft University of Technology, The Netherlands, August 29–September 2, 1983 (see also Lawrence Livermore National Laboratory, UCRL-88495 Rev. 1).

[44] S.T. Chan, H.C. Rodean, D.L. Ermak, Numerical Simulation of Atmospheric Releases of Heavy Gases Over Variable Terrain, Air Pollution Modeling and Its Applications III, vol. 5, Plenum Press, New York, 1984, pp. 295–328.

[45] D.L. Ermak, S.T. Chan, D.L. Morgan, L.K. Morris, A comparison of dense gas dispersion simulations with the Burro series LNG spill test results, J. Hazard. Mater. 6 (1–2) (1982) 129–160.